



Modern seismological reassessment and tsunami simulation of historical Hellenic Arc earthquakes

C.W. Ebeling^{a,*}, E.A. Okal^a, N. Kalligeris^b, C.E. Synolakis^{c,d}

^a Department of Earth and Planetary Sciences, Northwestern University, 1850 Campus Drive, Evanston, IL 60208, USA

^b Technical University of Crete, Chanea, Crete 73100, Greece

^c Department of Civil Engineering, University of Southern California, Los Angeles, CA 90089, USA

^d Hellenic Center for Marine Research, Anavyssos 19013, Greece

ARTICLE INFO

Article history:

Received 26 May 2011

Received in revised form 20 December 2011

Accepted 23 December 2011

Available online 2 January 2012

Keywords:

Earthquake

Hazard

Hellenic Arc

Magnitude

Relocation

Tsunami

ABSTRACT

Neither large magnitude nor tsunamigenic earthquakes occur frequently in the eastern Mediterranean, hampering comprehensive study of these events and consequential hazards whenever digital data are required. Using analog seismograms, travel-time catalogs, and hydrodynamic simulations, we reassess here four large ($M \sim 7$) historical earthquakes occurring in various regions of the Hellenic Arc: on 6 October 1947, in the Peloponnesus; 9 February 1948, near Karpathos; and a couplet east of Rhodos on 24 and 25 April 1957. Damaging near-field tsunamis are associated with the 1947 and 1948 earthquakes. Results include seismic moments (in units of 10^{27} dyn·cm) of 1.26 (1947), 0.97 (1948), 0.56 (1957a), and 1.09 (1957b); recovered focal mechanisms and hypocentral locations are consistent with the regional stress field resulting from the ongoing collision between the Nubia plate and Aegea microplate. Seismological reassessments indicate that the sources of the 1947 and 1948 tsunamis involved submarine slumping; hydrodynamic simulations assuming a submarine landslide source for the 1948 tsunami recreate run-up and inundation values consistent with eyewitness accounts presented here. Hydrodynamic simulations also show that the 25 April 1957 earthquake likely generated an unobserved tsunami with a maximum 50 cm run-up in Rhodos.

© 2011 Elsevier B.V. All rights reserved.

1. Introduction

Comprehensive understanding of large tsunamigenic eastern Mediterranean earthquakes and consequential tsunami hazard is hindered by the absence of such events after digital recording began in the 1980s. Using analog seismograms, Okal et al. (2009) studied the 1956 Amorgos earthquake, the largest to affect Greece during the last 100 years, and its associated tsunami. Here we extend their work to four other large Hellenic Arc earthquakes: in the southwestern Peloponnesus on 6 October 1947, near Karpathos on 9 February 1948, and two east of Rhodos on 24 and 25 April 1957 (Fig. 1(b)); these represent the only other shallow ($h < 70$ km) events in the Aegean region assigned a Pasadena magnitude M_{PAS} greater than $6\frac{7}{8}$ as defined by Gutenberg and Richter (1954).

Significant tsunamis were associated with the events of 1947 and 1948. While the targeted events have been mentioned in previous seismological studies (e.g. Abe, 1981; Ambraseys, 2001; Ambraseys and Jackson, 1990; Gutenberg and Richter, 1954; Makropoulos, 1978; McKenzie, 1972; Papazachos and Delibasis, 1969; Ritsema, 1974), our reassessment of these earthquakes is motivated both by the scatter in

published locations, depths, and focal geometries, and by the absence of seismic moments obtained using modern seismological techniques.

A notable gap also exists in the understanding of the 1947 and 1948 tsunamis, and of these four earthquakes as tsunami sources. We address this by using hydrodynamic simulations based on our seismological reassessments; run-up and inundation measurements based on eyewitness accounts further constrain our 1948 tsunami simulation. Even though no tsunami has been linked to either 1957 earthquake, these events may have been large enough to generate observable tsunamis on Rhodos and perhaps on the southwest coast of Turkey.

1.1. Tectonic setting

The eastern Mediterranean region (Fig. 1(a)) contains the Anatolia, Arabia, and Nubia plates, and the Aegea microplate, which moves 30 ± 1 mm/yr to the southwest relative to Eurasia (McClusky et al., 2000, 2003) and at a slightly lower velocity to the southwest relative to Nubia (Kreemer and Chamot-Rooke, 2004; Reilinger et al., 2006). Major regional tectonic features include the 9 ± 1 mm/yr left-lateral strike-slip East Anatolia Fault in eastern Turkey (McClusky et al., 2000, 2003) and the 24 ± 1 mm/yr right-lateral strike-slip North Anatolia Fault in northern Turkey (McClusky et al., 2000, 2003). The system is dominated by the Hellenic Arc and trench

* Corresponding author. Tel.: +1 847 467 1639; fax: +1 847 491 8060.
E-mail address: carl@earth.northwestern.edu (C.W. Ebeling).

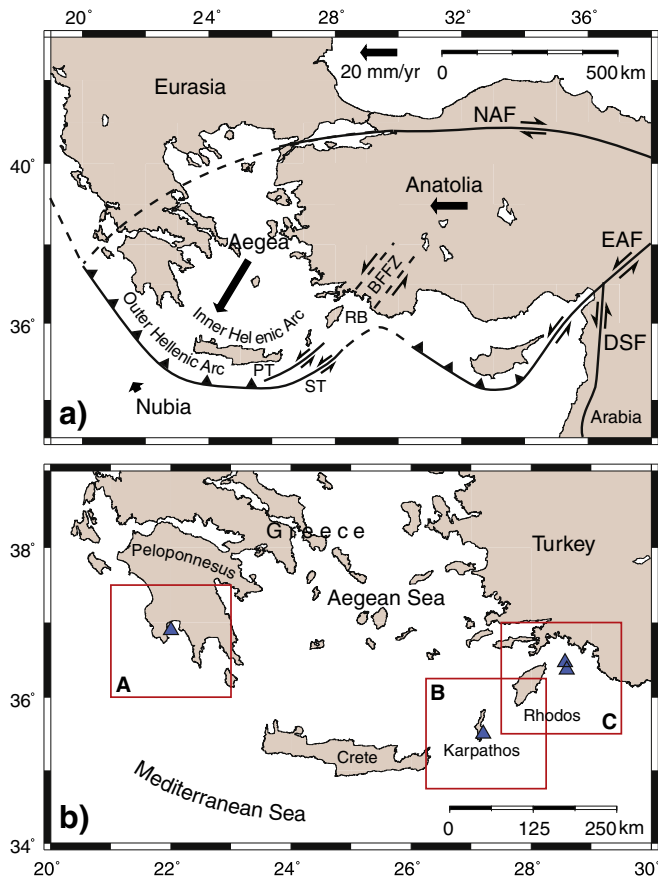


Fig. 1. (a) Simplified tectonic map showing the eastern Mediterranean region, after Hall et al. (2009), Jackson (1994), Jongsma (1977), McClusky et al. (2000, 2003), and Reilinger et al. (2006). BFFZ = Burdur-Fethiye Fault Zone; DSF = Dead Sea Fault; EAF = East Anatolian Fault; PT = Pliny Trench; RB = Rhodos Basin; ST = Strabo Trench. Lines indicate faults (dashed when inferred). Teeth on overriding plate show thrust fault; sense of motion shown by half-arrows when strike-slip. Solid arrows show velocities relative to Eurasia. (b) Map showing International Seismological Summary (ISS) locations of events included in this study. Box A: 6 October 1947 event; B: 9 February 1948; C (south): 24 April 1957; and C (north): 25 April 1957. Areas outlined in red correspond to maps in Figs. 3(a), 4(a), 5(a), and 6(a).

(LePichon and Angelier, 1979), along which Nubia Neo-Tethys oceanic lithosphere subducts northward under southern Aegea.

Aegea tectonics are characterized by 35–40 mm/yr north–south extension in central and southern Aegea (Kiritzi and Louvari, 2003; Kiritzi and Papazachos, 1995; LePichon and Angelier, 1979; McClusky et al., 2000; McKenzie, 1978); east–west extension in the inner Hellenic Arc (Kreemer and Chamot-Rooke, 2004; McClusky et al., 2003); and thrust faulting in the outer Hellenic Arc (Benetatos et al., 2004; McKenzie, 1972, 1978). Roll-back of the subducting Nubia slab plays an influential kinematic role by inducing Aegea to move towards the Hellenic trench (Bohnhoff et al., 2005; Reilinger et al., 2006).

Nubia-Aegea relative plate motion at the Hellenic Arc, directed ~N45°E (Bohnhoff et al., 2005), results in convergence varying from nearly arc-orthogonal in the west to left-lateral arc-oblique in the east. While evidence exists for large vertical displacements across the northeast–east–northeast-trending deep-sea depressions on the eastern limb of the arc known as the Pliny and Strabo trenches (Jongsma, 1977), it is primarily left-lateral strike-slip motion arising from arc-oblique convergence that is accommodated by these structures (Kreemer and Chamot-Rooke, 2004; LePichon and Angelier, 1979; LePichon et al., 1995). The western terminus of the Pliny and Strabo trenches lies southeast of Crete. While their eastern terminations are not well defined, a broad Pliny-Strabo zone of deformation

has been correlated with the Burdur-Fethiye Fault Zone in southwestern Turkey (Hall et al., 2009).

2. Methodologies and data sets

2.1. Event relocation

We used the interactive and iterative Monte Carlo relocation algorithm of Wyession et al. (1991) to relocate events. Relocations were carried out using *P*-wave arrival time data published by the International Seismological Summary (ISS) from stations located at epicentral distances up to 100° (Table 1). Uncertainties in relocation arise from station timing errors and bias in station coverage, which is best in the east and northeast, where stations located in Japan and east Asia dominate; and in the northwest quadrant, where a large number of stations in Europe and North America are located. To replicate timing uncertainties typical of the 1940s and 1950s, randomly-generated Gaussian noise ($\sigma_c = 3\text{--}5$ s) was included in arrival time data sets. The resulting 95% confidence ellipse expresses a relocation's reliability.

2.2. Preliminary determination of focal mechanism (PDFM) inversion

To recover fault plane solutions and seismic moments, we used the Preliminary Determination of Focal Mechanism (PDFM) method (Reymond and Okal, 2000), which inverts mantle Rayleigh and Love wave spectral amplitudes. This method is ideal for use with sparse data sets made up of historical records in that it does not rely on erroneous or non-existent time corrections and instrument polarities. It is robust for data sets consisting of only a few records, given sufficient azimuthal coverage (Reymond and Okal, 2000), and is largely insensitive to uncertainties in epicentral estimates (Okal and Reymond, 2003). But because the PDFM algorithm does not use phase information (Okal and Reymond, 2003; Reymond and Okal, 2000; Romanowicz and Suárez, 1983), it results in indeterminacies in fault strike ϕ , in which the entire fault plane solution can be rotated 180° in the horizontal plane, and in the sense of slip on the fault, which can be reversed by adding 180° to the slip angle λ while fault strike ϕ and dip δ remain the same.

Indeterminacies were resolved using body-wave polarities and relative amplitudes recorded at the stations used in PDFM inversions and at De Bilt, Netherlands (DBN) and Vienna, Austria (VIE). Seismograms from these regional stations were not used in inversions because epicentral distances did not allow sufficient temporal separation of Love and Rayleigh wavetrains.

Centroid depths for these events were obtained by minimizing root-mean-square residuals of PDFM inversions at depths constrained between 10 and 100 km.

The analog seismograms came from the Benioff 1–90 seismometer at Pasadena, California (PAS); the McRomberg tilt-compensating seismometer at College, Alaska (COL); the Milne-Shaw seismometer at Honolulu, Hawaii (HON); and Wenner seismometers at Huancaayo, Peru (HUA) and San Juan, Puerto Rico (SJG) (Fig. 2). High-quality first-passage Love (G_1) and Rayleigh (R_1) wavetrains in these seismograms were digitized and equalized to a 1 Hz sampling rate. Digitized records were corrected for instrument response, magnification, and damping, using instrument constants as described in Charlier and van Gils (1953). Stations used in PDFM inversions are listed in Table 2.

3. Results

3.1. Southwest Peloponnese, 6 October 1947 (1947:279)

3.1.1. Background and previous work

The earthquake of October 6, 1947 resulted in severe damage, three deaths, and over 20 injuries in the southwestern Peloponnese Galanopoulos (1949). A tsunami associated with this event inundated Methoni, a coastal town on the Mediterranean Sea, from 15 m to 60 m

Table 1

Previous origin times, epicentral locations, and depths, with relocation results for four study events. Number of stations used in relocation inversions, standard deviations of Gaussian noise (σ_G) injected into arrival time data sets, and standard deviations of P -travel times from relocations (σ_P) are listed in rightmost three columns.

Event (YYYY:JJJ)	Month	Day	Time (GMT)	Lat. (°N)	Lon. (°E)	Depth (km)	Source	No. stations	σ_G (s)	σ_P (s)
1947:279	Oct	6	19:55:34 19:55:42	36.9 37.04	22.0 21.76	28 57 + 2/– 15	ISS This study	108	5	3.9
1948:040	Feb	9	12:58:13 12:58:23	35.5 35.80	27.2 27.19	– 60 + 15/– 10	ISS This study	108	4	2.1
1957:114	Apr	24	19:10:13 19:10:12	36.37 36.31	28.59 28.62	48 40 + 15/– 5	ISS This study	243	3	2.7
1957:115	Apr	25	02:25:42 02:25:41	36.47 36.40	28.56 28.55	53 41 ± 15	ISS This study	265	3	2.5

(Ambraseys and Jackson, 1990; Galanopoulos, 1949). Papadopoulos and Chalkis (1984) report a 15 m inundation at an unnamed location. Soloviev (1990) lists a submarine landslide triggered by the earthquake as the probable tsunami source.

This part of Greece has some history of large ($6.5 < M < 7.5$) events, with five in the last two centuries. Epicenters of strong ($M_s \geq 6.0$) events fall along the southwestern coast of the Peloponnese (Papazachos, 1996). Although this region is characterized by a nearly horizontal north- to northeast-trending maximum compressive stress field (Kiratzi and Papazachos, 1995; McKenzie, 1972, 1978; Papadopoulos et al., 1986; Papazachos et al., 1999), both normal- (Ambraseys and Jackson, 1990; Papazachos and Delibasis, 1969) and thrust-dominated (Papazachos et al., 1997) focal mechanisms for this event have been proposed.

3.1.2. Relocation

Inversion of P -wave travel times shifts the origin time + 9 s from the ISS origin time (Table 1). The relocation yields a location ~30 km northwest of the ISS location, and moves the epicenter from

the Gulf of Messinia to the southwest Peloponnese (Fig. 3(a)). The 95% location uncertainty ellipse lies mostly on land and does not include the ISS location. Because the depth did not converge using the Monte Carlo routine, we fixed it to that obtained in the PDFM inversion to relocate the event.

3.1.3. PDFM moment and focal mechanism

The data set for the PDFM inversion comprised spectral amplitudes at periods between 51 and 170 s from five G_1 and four R_1 wavetrains from five stations with an aperture of 95° in azimuth (Table 2). The PDFM inversion converges on a moment (Table 4) considerably greater than the only previously-published value of 2.95×10^{26} dyn·cm (Ambraseys, 2001), calculated from M_s values following Ekström (1987). The fit of measured spectral amplitudes to theoretical radiation patterns for our preferred solution is shown in Fig. 3(b).

The 57 km PDFM centroid depth minimizes RMS residuals (Table 1 and Fig. 3(c)). Because shallower centroid depths are less constrained than those deeper, we assign a + 2/– 15 km uncertainty. This depth is deeper than previously-published values: the ISS published a depth of 28 km, and based on macroseismic observations, Galanopoulos (1949) proposed a depth between 28 and 42 km.

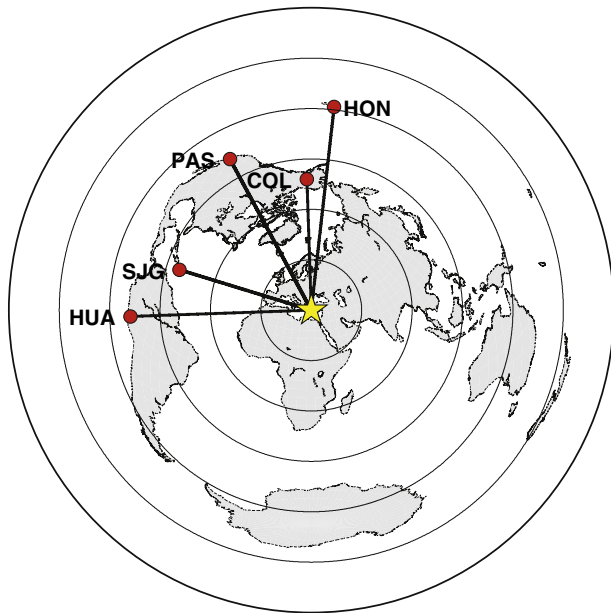


Fig. 2. Great-circle travel paths between stations used in PDFM inversion and event of 6 October 1947; epicenter shown by yellow star. Concentric circles are at 30° increments. Not every station mix used in PDFM inversion for other three events was the same as this group, but the locations of all stations used are shown. Stations (red circles) are located at College, Alaska (COL); Honolulu, Hawaii (HON); Huancayo, Peru (HUA); Pasadena, California (PAS); and San Juan, Puerto Rico (SJG). Epicentral distances depend on event and range from about 78° to 122° ; azimuthal coverage extends from about 267° to 360° .

Table 2

Seismological data set used in PDFM inversions.

Event (YYYY:JJJ)	Station location	Station code	Dist. (°)	AZ (°)	BAZ (°)	Comp.	Wavetrain
1947:279	College, Alaska	COL	78.0	355.6	8.3	EW	G_1
						NS	R_1
	Honolulu, Hawaii	HON	121.8	0.0	0.0	EW	G_1
	Huancayo, Peru	HUA	103.0	264.9	54.6	NS	G_1
						EW	R_1
1948:040	Pasadena, California	PAS	99.9	327.5	31.3	EW	G_1
						Z	R_1
	San Juan, Puerto Rico	SJG	77.8	283.7	54.9	NS	G_1
						EW	R_1
						EW	R_1
1957:114		COL	79.7	357.8	4.3	EW	G_1
						NS	R_1
		HUA	106.9	267.4	56.5	NS	G_1
						EW	R_1
		PAS	103.3	331.0	28.5	EW	G_1
1957:115						Z	R_1
		SJG	82.1	286.7	55.2	NS	G_1
		HUA	108.1	268.4	56.0	NS	G_1
						NS	R_1
		PAS	103.4	332.2	27.2	EW	G_1
1957:115						Z	R_1
		SJG	83.2	287.5	54.4	EW	G_1
						EW	R_1
		HUA	108.2	268.6	55.5	NS	G_1
		PAS	103.0	332.3	26.9	NS	G_1
					Z	R_1	
		SJG	83.1	287.5	53.9	EW	G_1
					EW	R_1	

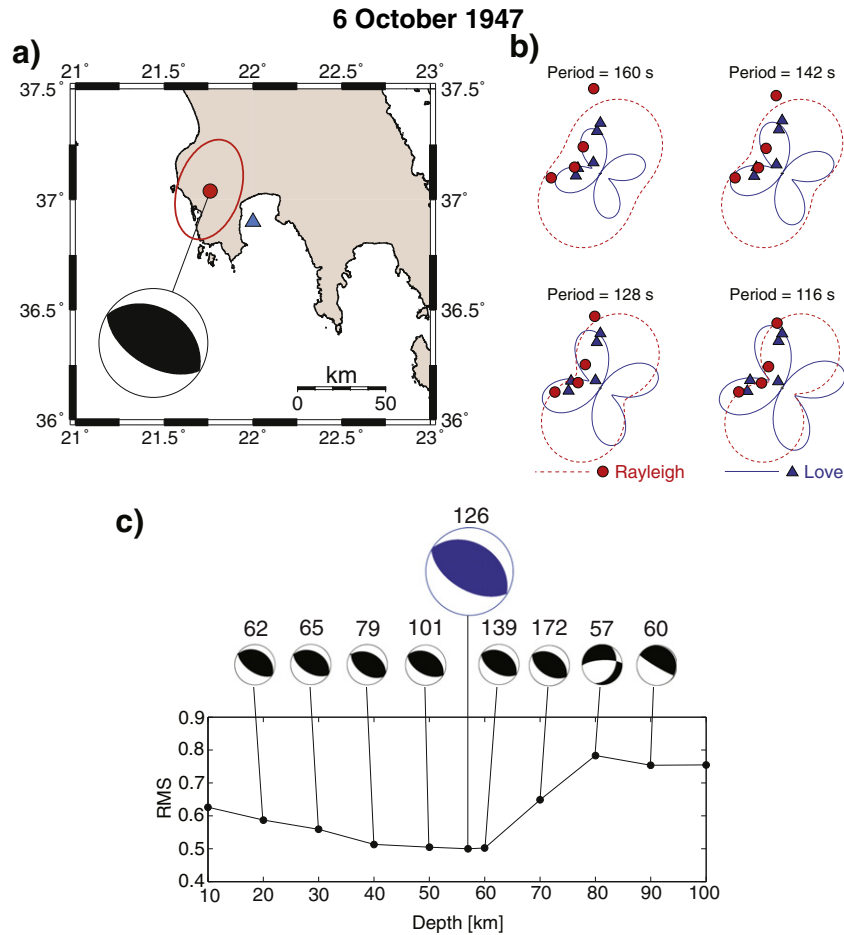


Fig. 3. Relocation and preferred PDFM focal mechanism (lower hemisphere projection) results for the 6 October 1947 event in the southwest Peloponnese. (a) Map corresponding to box A in Fig. 1(b) with ISS location as blue triangle; relocation and 95% confidence ellipse in red. (b) Rayleigh and Love wave radiation patterns as a function of azimuth for four periods; symbols and lines represent observed and theoretical spectral amplitudes, respectively. (c) Evolution by RMS value of PDFM focal mechanism and seismic moment M_0 as a function of centroid depth (in units of 10^{25} dyn·cm). Preferred solution is in blue.

Ambraseys (2001) reports a depth of 25 km obtained through the relocations of Makropoulos (1978).

A clear P arrival with positive polarity on the DBN vertical component, the only first-arrival record of this data set, resolves the indeterminacy in slip but not the 180° indeterminacy in strike. Two nearly pure thrust solutions remain, with the solid rotation between the two being 20° . We prefer the focal mechanism with the fault plane gently dipping to the northeast (Table 4), since DBN lies further away from the node in this solution. Focal mechanisms recovered by the PDFM inversion for depths between 42 and 59 km are very consistent with our preferred solution, falling within a 5° range of solid rotation (Fig. 3(c)). This range can be regarded as a confidence interval for our solutions.

Ambiguity is associated with the previously-published normal-dominated focal mechanisms. Ambraseys and Jackson (1990) assign theirs based on this event's geographical proximity to the Kalamata earthquake of 13 September 1986. Papazachos and Delibasis (1969) list a solution defined by the type of faulting on a system of two planes consistent with a double-couple source but with non-double-couple compression and tension axes. Our mechanism is compatible with the more credible thrust-dominated solution of Papazachos et al. (1997). It is consistent with a thrust event at the interface between the Aegea microplate and the subducting Nubia plate, which dips $\sim 30^\circ$ to the east-northeast beneath the western Peloponnese at this depth (Papazachos et al., 2000).

3.2. Karpathos, 9 February 1948 (1948:040)

3.2.1. Background and previous work

The tsunami associated with the Karpathos earthquake of 9 February 1948 inundated 900 m at an unnamed location (Papadopoulos and Chalkis, 1984). Papadopoulos et al. (2007) report eyewitness accounts of an initial sea withdrawal at Pigadia Bay 5 to 10 min after the earthquake; a subsequent 250-m inundation there, which resulted in extensive damage to vessels and homes; and inundation at the town of Finiki, on the southwest coast of Karpathos. However, we note that Ambraseys and Synolakis (2010) have critically re-examined the catalog entries of Papadopoulos et al. (2007) and concluded that some may be spurious, but have nonetheless been uncritically copied in subsequent derivative works.

The frequency of strong ($M_s \geq 6.0$) earthquakes in this region is low; no events with $M_s > 7.1$ are known, but the frequency of $5.5 < M_s < 5.9$ events since 1911 is high (Papazachos, 1996). The area in which this event occurred is dominated by oblique subduction, with nearly horizontal northeast-southwest-trending maximum compressive stress axes (Kiritzi and Papazachos, 1995; Papadopoulos et al., 1986). The one published focal mechanism that we find, determined using P -wave polarities, is thrust-dominated with a significant component of strike-slip motion (Papazachos and Delibasis, 1969). However, this mechanism is characterized by a double-couple two-plane solution with non-double-couple compression and tension axes.

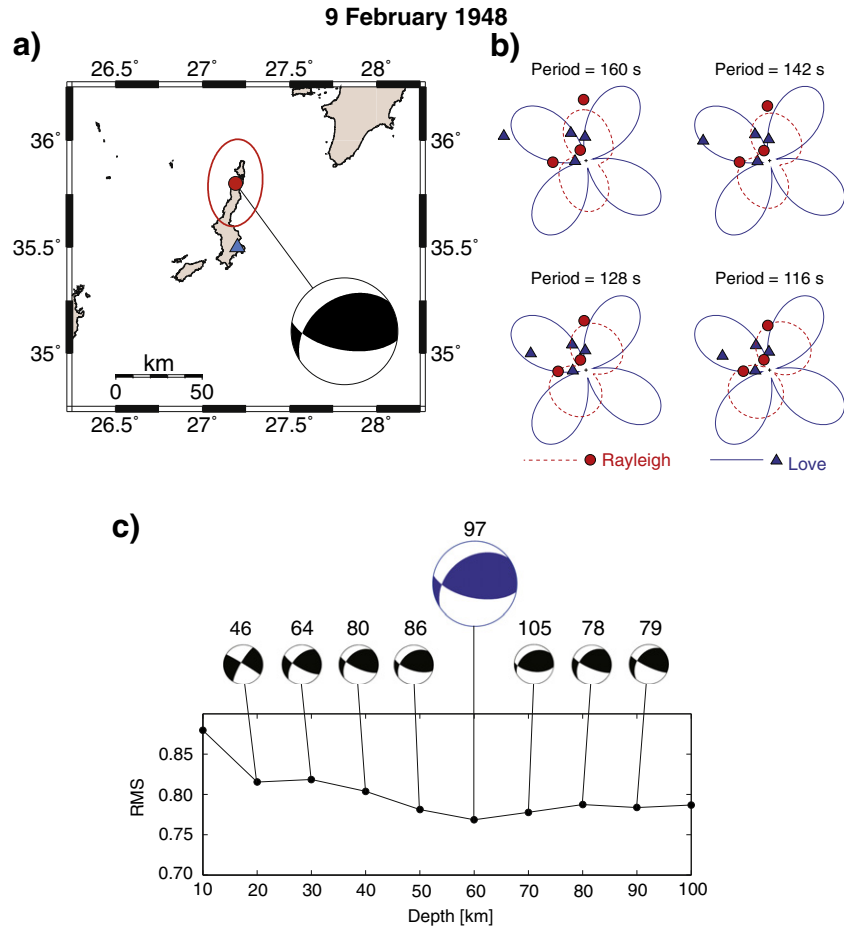


Fig. 4. Same as Fig. 3 but for Karpathos event of 9 February 1948. Map area in (a) corresponds to box B in Fig. 1 (b).

3.2.2. Relocation

Inversion of P travel times shifts the origin time +10 s from the ISS origin time (Table 1). The relocation represents a change of ~33 km to the north of the ISS location, and moves the epicenter to the northern tip of the island (Fig. 4(a)). Although the relocated epicenter is on land, the majority of the 95% confidence ellipse is over water and does not include the ISS location. Because the depth did not converge using the Monte Carlo routine, we fixed it to the value obtained in the PDFM inversion to relocate the event.

3.2.3. PDFM moment and focal mechanism

Our PDFM data set included spectral amplitudes at periods between 51 and 205 s from four G_1 and three R_1 wavetrains from four stations providing an aperture of 90° in azimuth (Table 2). The PDFM inversion converges on a moment (Table 4) comparable to the value of 6.76×10^{26} dyn·cm Ambraseys (2001) calculated from M_s values following Ekström (1987). The fit of measured spectral amplitudes to theoretical radiation patterns based on our preferred solution is shown in Fig. 4(b).

The 60 km PDFM centroid depth (Table 1 and Fig. 4(c)) minimizes RMS residuals. Because deeper centroid depths are slightly less constrained than those shallower, we assign a +15/−10 km uncertainty. This depth is significantly deeper than the 40 km and 30 km reported by Gutenberg and Richter (1954) and Makropoulos (1978), respectively.

The indeterminacy between the four possible focal mechanisms is resolved using a positive P -arrival polarity on the vertical component at PAS; first-motion P arrivals at COL to the south and at SJG to the

south and east, at both stations away from the event; a SH polarity to the west at COL; a COL SV/SH amplitude ratio ~1; and an obvious S -wave amplitude difference on the horizontal components at SJG, with the east–west \gg north–south. Our preferred solution is thrust-dominated with a strike-slip component (Table 4). Focal mechanisms recovered by the PDFM inversion for depths between 50 and 75 km are very consistent with this solution, falling within 8° of solid rotation (Fig. 4(c)).

Our solution is compatible with an event at the interface between the Aegea microplate and the subducting Nubia plate, which dips ~30° to the northwest in this region (Papazachos et al., 2000).

3.3. East of Rhodos, 24 April 1957 (1957:114)

3.3.1. Background and previous work

Published focal mechanisms for this event are predominantly strike-slip with varying amounts of normal (Ritsema, 1974) and thrust (McKenzie, 1972; Papazachos and Delibasis, 1969) motion. Left-lateral motion for these three solutions on east- to northeast-trending faults is consistent with a maximum compression direction trending northeast–southwest (McKenzie, 1972). It is nearly horizontal for the solutions of McKenzie (1972) and Papazachos and Delibasis (1969), whereas the compression axis of Ritsema (1974) plunges ~35° to the south-southeast. Papazachos (1996) characterizes this region with a nearly pure thrust focal mechanism reflecting maximum compression trending similarly but plunging ~20° to the southwest.

Although both this event and that of the following day (discussed below) occurred in a source region of a number of probable or likely tsunamis (Altınok and Ersoy, 2000; Soloviev, 1990), including perhaps that

of the 1303 tsunami (Ambraseys and Synolakis, 2010; El-Sayed et al., 2000; Guidoboni and Comastri, 1997; Papazachos, 1996), we have been unable to locate records of a tsunami associated with either event of April 1957.

3.3.2. Relocation

Inversion of P travel times shifts the origin time only -1 s from the ISS origin time (Table 1). The relocation yields a change of ~ 7.5 km to the south-southeast of the ISS location. Both the ISS and relocated epicenters lie in the Mediterranean Sea; the 95% confidence ellipse includes the ISS location (Fig. 5(a)). The depth converged to 36 km using the Monte Carlo routine.

3.3.3. PDFM moment and focal mechanism

The PDFM data set included spectral amplitudes at periods between 51 and 205 s from three G_1 and three R_1 wavetrains from three stations providing an aperture of 64° in azimuth (Table 2). The PDFM inversion converges on a well-constrained moment (Table 4) significantly greater than the value of 9.33×10^{25} dyn·cm (Ambraseys, 2001) from M_s values following Ekström (1987). The fit of measured spectral amplitudes to theoretical radiation patterns for our preferred solution is shown in Fig. 5(b).

The PDFM centroid depth of 40 km minimizes RMS residuals (Fig. 5(c)). Because deeper centroid depths are less constrained than those shallower, we assign a $+15/-5$ km uncertainty. This depth is comparable to the 36 km from the Monte Carlo relocation and to the 40 km of Ambraseys (2001) based on relocations by Makropoulos (1978). It is significantly shallower than the 48 km reported by the ISS, the 50 km preferred by McKenzie (1972), and

the 69 ± 5 km of Makropoulos and Burton (1981). Only the latter falls outside our depth uncertainty range.

Of the four possible focal mechanisms, only our nearly pure strike-slip preferred solution (Table 4) predicts correctly both the positive (upward) P polarity on the DBN vertical component and the polarity of the S arrivals to the west and south on the DBN horizontal components. Our solution thus falls in the group of Papazachos and Delibasis (1969), McKenzie (1972), and Ritsema (1974). Focal mechanisms recovered by the PDFM inversion for depths between 35 and 55 km are generally consistent with our preferred solution, falling within a 14° range of solid rotation (Fig. 5(c)).

3.4. East of Rhodes, 25 April 1957 (1957:115)

3.4.1. Background and previous work

This event took place about five hours after the event of 24 April at a similar location. Except for the nearly pure thrust mechanism on northwest-southeast-trending fault planes of Papazachos (1996) and Papazachos et al. (1999), published focal mechanisms are predominantly strike-slip with fault planes trending northeast-southwest and northwest-southeast (McKenzie, 1972; Papazachos and Delibasis, 1969; Ritsema, 1974), similar in both mechanism and orientation to solutions for the event of the previous day.

3.4.2. Relocation

Inversion of P travel times shifts the origin time -1 s from the ISS origin time (Table 1). The relocation represents a change of ~ 8 km to the south-southwest of the ISS location (Fig. 6(a)). Both the ISS and relocated epicenters lie in the Mediterranean Sea; the ISS location is

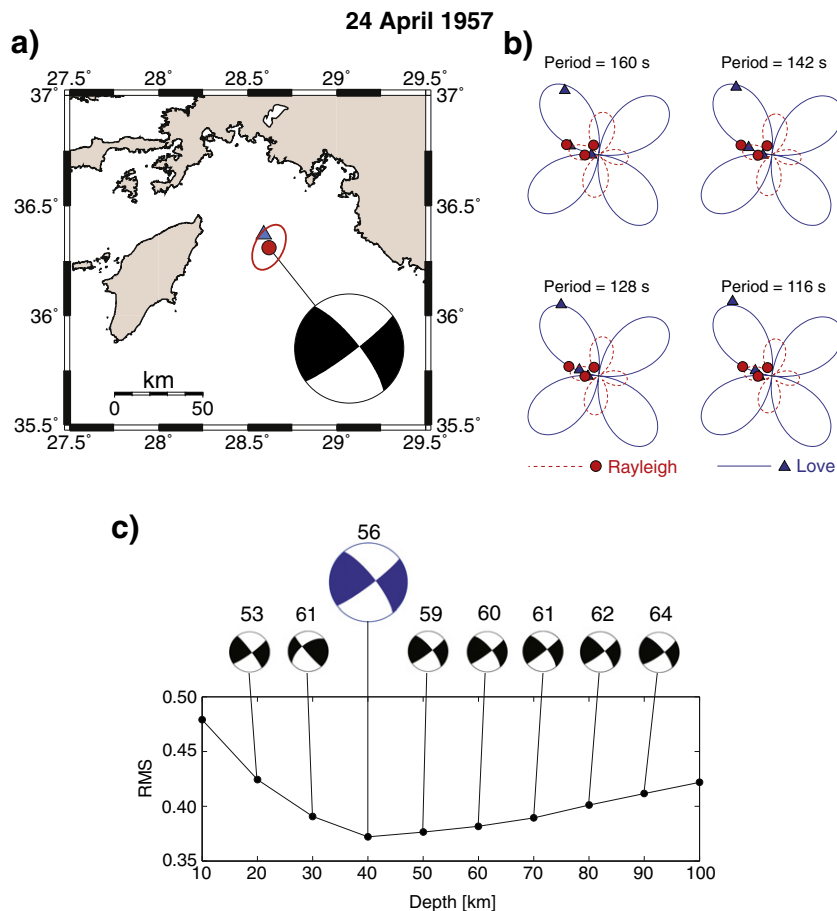


Fig. 5. Same as Fig. 3 but for 24 April 1957 event east of Rhodes. Map area in (a) corresponds to box C in Fig. 1(b).

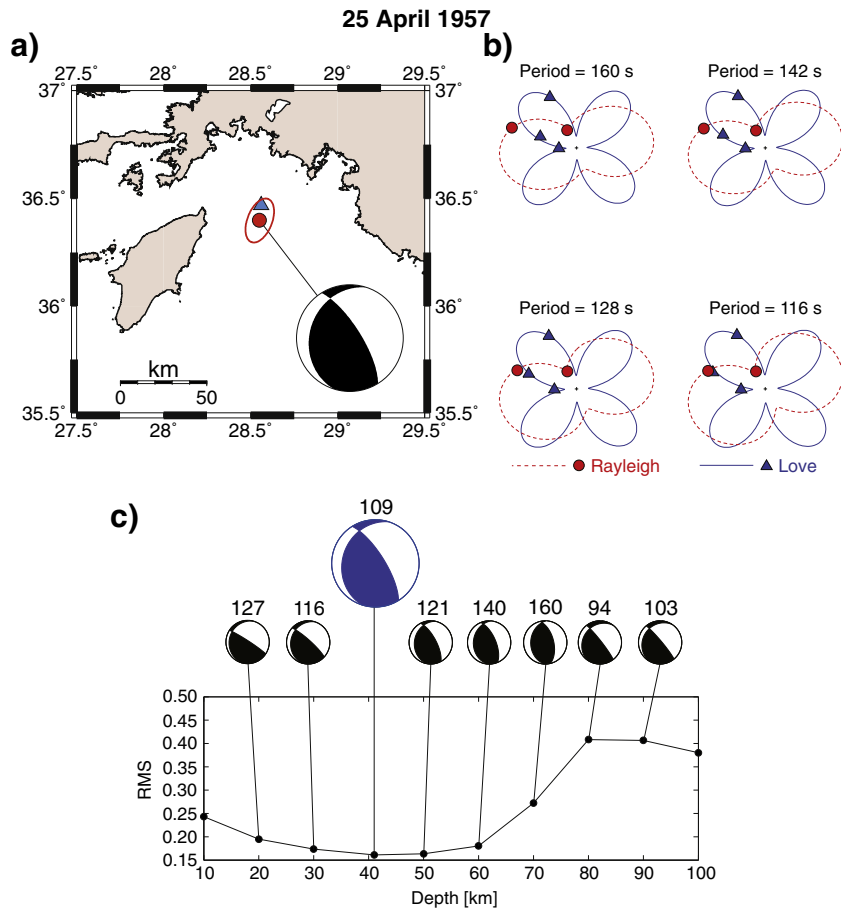


Fig. 6. Same as Fig. 3 but for 25 April 1957 event east of Rhodes. Map area in (a) corresponds to box C in Fig. 1(b).

included in the 95% confidence ellipse. The depth converged to 36 km using the Monte Carlo routine with a floating depth.

3.4.3. PDFM moment and focal mechanism

The PDFM data set included spectral amplitudes at periods between 51 and 170 s from three G_1 and two R_1 wavetrains from three stations providing an aperture of 64° in azimuth (Table 2). Our moment (Table 4) is the first that we are aware of for this earthquake. The fit of measured spectral amplitudes to theoretical radiation patterns based on our preferred solution is shown in Fig. 6(b).

The 41 km PDFM centroid depth minimizes RMS residuals (Fig. 6(c)). Because deeper and shallower centroid depths are

Table 3
9 February 1948 tsunami survey data set on Karpathos. See Fig. 7 for maximum run-up map locations.

Number	Latitude (°N)	Longitude (°E)	Amplitude (m)	Nature ^a	Comment
<i>Pigadia</i>					
1	35.5081	27.2147	>2.9	FD	Fountain on square overtopped
2	35.5069	27.2152	7	R	Taxi square
3	35.5080	27.2142	5.7	WM	National bank building
4	35.5079	27.2123	4	R	Private home
<i>Agia Kara</i>					
5	35.5273	27.1968	7.3	R	Olive trees, 200 m inland
<i>Diafani</i>					
6	35.7552	27.2105	3.1	R	House porch
7	35.7553	27.2096	3.6	R	Creek bed, 200 m inland

^a FD: Flow depth; R: Run-up; WM: Water mark.

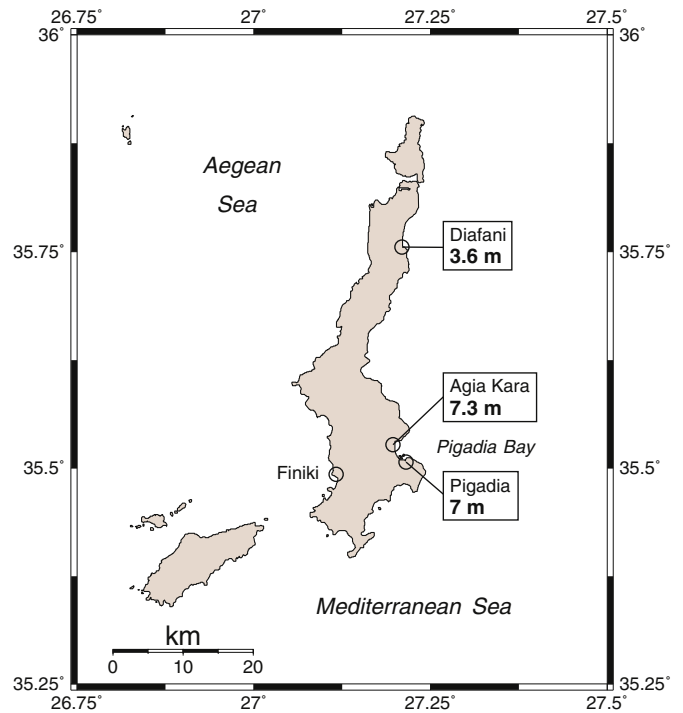


Fig. 7. Maximum tsunami run-up associated with 9 February 1948 earthquake on the island of Karpathos from eyewitness accounts. No recollections of run-up or inundation at Finiki (located on southwest coast of island) were recorded. Relocated epicenter is at northern tip of island approximately 10 km north of Diafani.

constrained equally, we assign a ± 15 km uncertainty. This centroid depth is consistent with that recovered by the Monte Carlo relocation routine, and the 53 km depth reported by the ISS falls within our depth range. The 20 km reported by Ambraseys (2001) based on relocations by Makropoulos (1978), however, does not.

The indeterminacy between the four possible focal mechanisms is lifted using a positive P -wave polarity on the DBN vertical component; P -wave arrival polarities on the SJG horizontal components to the south and west, away from the event; and a negative P -wave polarity on the VIE vertical component (although its amplitude is unexpectedly large for a station located $\sim 7^\circ$ from the null axis). Our preferred solution (Table 4) is thrust-dominated with a small dip-slip component. Focal mechanisms recovered by the PDFM inversion for depths between 26 and 56 km are generally consistent with this solution, falling within 34° of solid rotation (Fig. 6(c)).

4. Tsunami of 9 February 1948

4.1. Field survey

The island of Karpathos was visited in 2008 by two of the authors (N.K. and C.E.S.) during the field survey of the 1956 Amorgos tsunami (Okal et al., 2009), which provided an opportunity to interview witnesses of the 1948 event. The possibility of confusion in witness memory between the two events is eliminated by their distinctly different times of occurrence (afternoon and dawn for the 1948 and 1956 events, respectively). Our resulting data set (summarized in Table 3 and Fig. 7) is built on the testimony of seven witnesses, aged 10 to 32 at the time of the 1948 tsunami, from interviews following established procedures developed by International Tsunami Survey Teams (Synolakis and Okal, 2005).

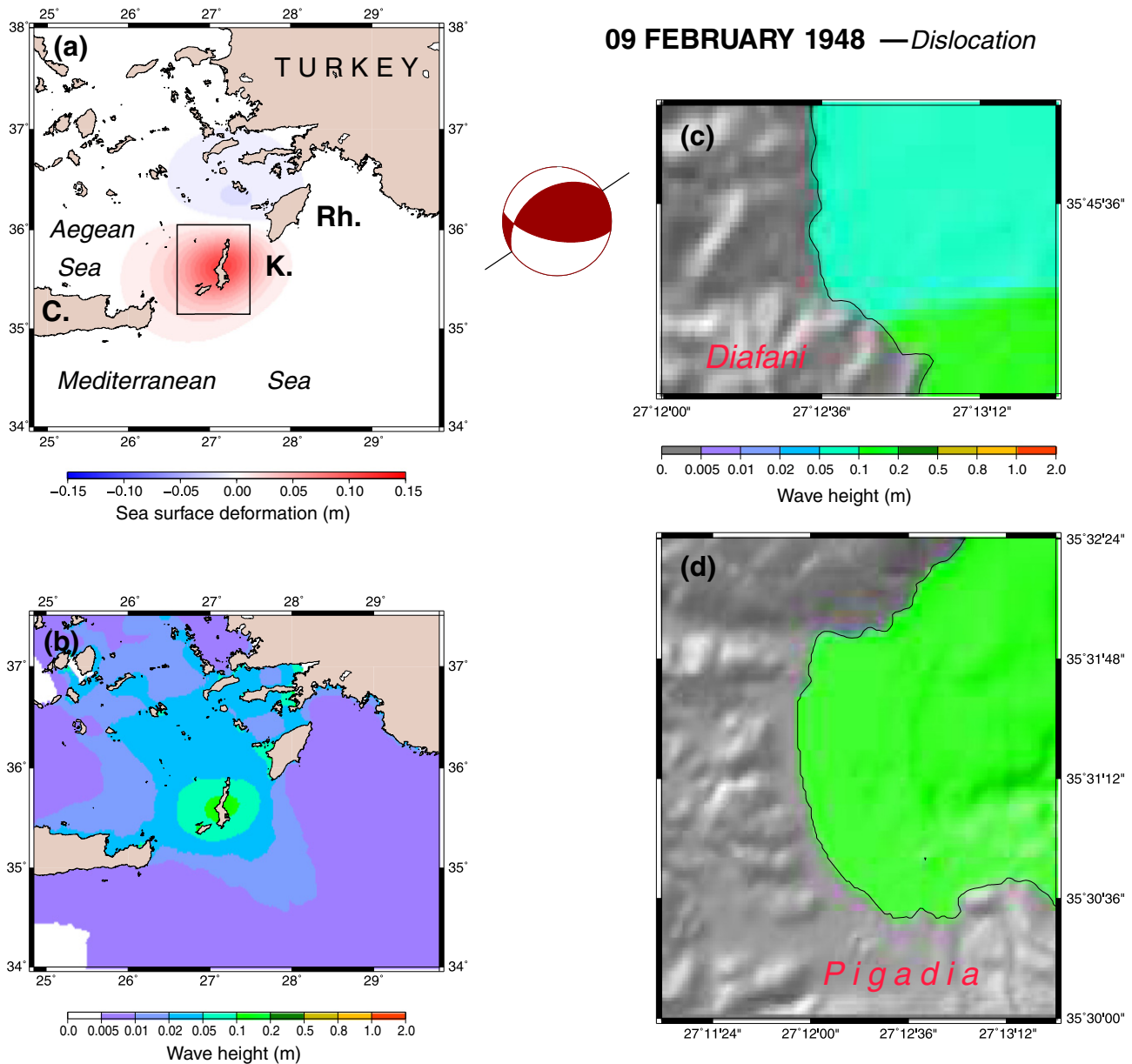


Fig. 8. Hydrodynamic simulation results for tsunami generated by 9 February 1948 earthquake on northwest-dipping fault plane of preferred focal mechanism (identified on beachball). (a) Regional vertical sea surface deformation calculated after Okada (1985) using scaled fault geometry Geller, 1976 and inverted moment; C. = Crete; K. = Karpathos; Rh. = Rhodes. Box around Karpathos represents Fig. 9(a) map area. (b) Regional contour map showing maximum tsunami amplitude at each simulation point. Small boxes on east coast of Karpathos at Diafani (north) and Pigadia (south) in subfigures (a) and (b) represent grids sampled at 50 m in simulations. Contour maps of maximum tsunami amplitude at Diafani and Pigadia are shown in (c) and (d), respectively; small boxes in (a) and (b) are identical to these map areas.

All four witnesses in Pigadia recalled a leading depression that dried the > 15 m deep channel separating the small Pigadia Bay island of Despotiko from the mainland. The water then rose to penetrate as far as 200 m inland and reached the present taxi square, 7 m above mean sea level, along an open channel since paved over.

In Agia Kara, the waves overtopped the local road and inundated olive trees located 200 m inland at an altitude of 7.3 m.

The witness in Diafani, aged 92 in 2008 but with a superb memory, recalled three waves following a leading sea depression at an estimated depth of 7 m. The witness indicated two inundation points at altitudes of 3.1 m on dry land, and 3.6 m in a creek bed.

These interviews complement the work of Papadopoulos et al. (2007), who obtained two data points in Pigadia with significantly lower amplitudes than confirmed by our survey. These authors report

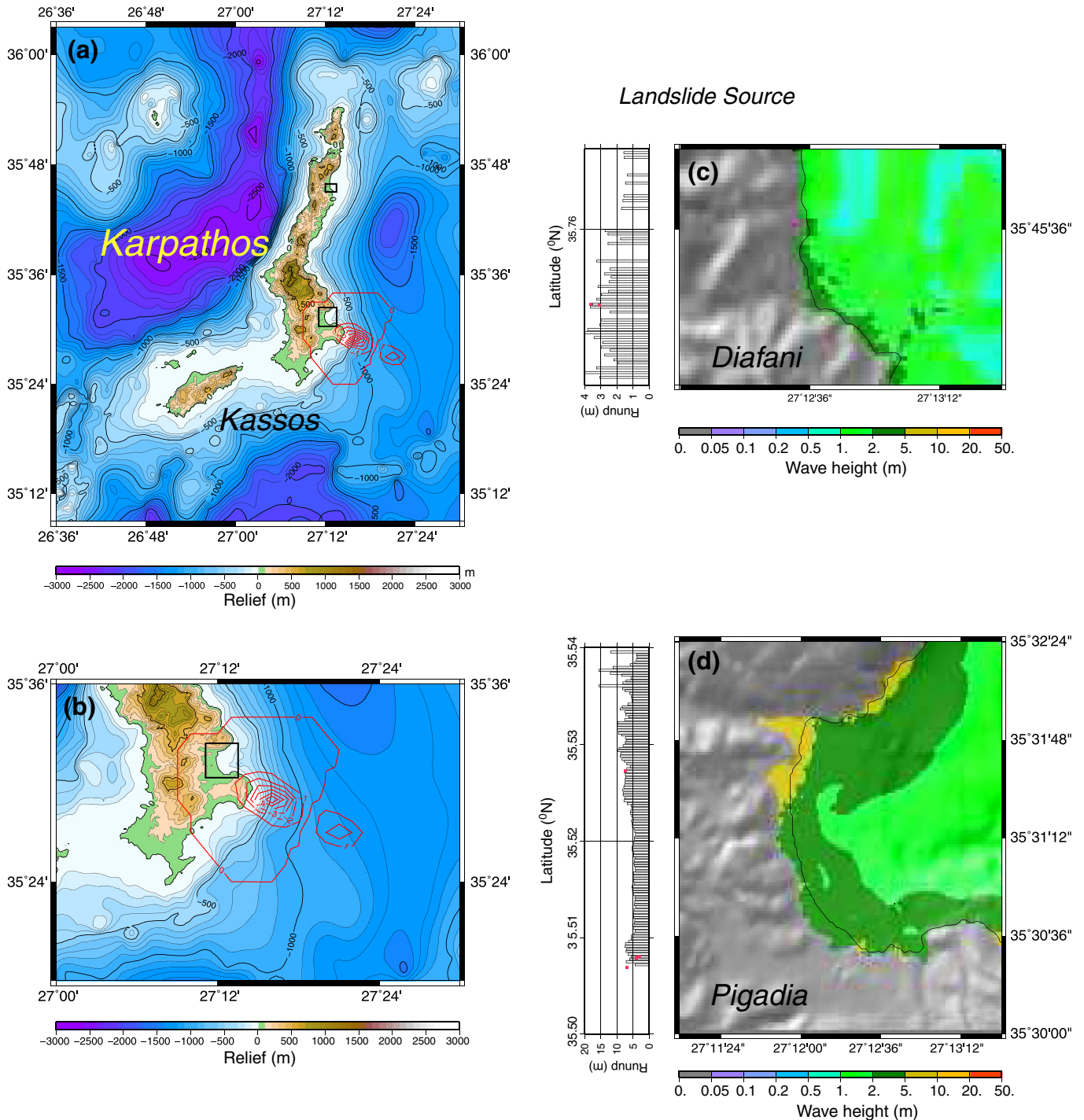


Fig. 9. Hydrodynamic simulation results for tsunami generated by submarine landslide triggered by 9 February 1948 earthquake. (a) Contoured topographic and bathymetric map showing initial vertical sea-surface deformation assuming dipole source; black contour interval 500 m. Contoured amplitude of dipole source shown in red; interval is 1 m. Source amplitude ranges from -6 m to $+2$ m. This map area shown by large box around Karpathos in Fig. 8(a). (b) Close-up of southern Karpathos showing landslide contours (red). Small boxes on east coast of Karpathos in subfigures (a) and (b) at Diafani (north) and Pigadia (south) represent grids sampled at 50 m in simulations. Contour maps of maximum tsunami amplitude at Diafani and Pigadia are shown in (c) and (d), respectively; red points in simulated run-up amplitude panels to the left of (c) and (d) represent survey measurements (see Fig. 7). Small boxes in (a) and (b) are identical to (c) and (d) map areas.

that the 1948 tsunami was also observed at Finiki, on the southwest coast of Karpathos. While we obtained a data point for the 1956 tsunami in Finiki (Okal et al., 2009), our witness there, who remembered the shaking during the 1948 earthquake, did not recall anomalous wave activity following it. We are thus unable to confirm that the 1948 tsunami reached the western coast of Karpathos.

5. Hydrodynamic simulations

In this section, we conduct hydrodynamic simulations of tsunamis generated by the 1948 earthquake near Karpathos and by the two 1957 events near Rhodos. Because the majority of the 95% location uncertainty ellipse lies on land and constraining run-up and inundation data are lacking, we do not carry out simulations for the 1947 Peloponnese tsunami.

We use scaling laws (Geller, 1976) to derive from each PDFM mechanism and seismic moment a fault geometry comprised of length L , width W , and slip S . This fault model is embedded into a homogeneous half-space. Using the formalism of Okada (1985), we then compute the resulting vertical static displacement field at the sea floor; this is assumed representative of initial conditions for the hydrodynamic simulation. For each earthquake, simulations are carried

out for both fault plane choices for the focal mechanisms inverted in Section 3.

The simulation is performed using the MOST (Method Of Splitting Tsunami) numerical code (Titov and Synolakis, 1998), which solves the non-linear equations of hydrodynamics under the shallow-water approximation using the method of alternate steps. A series of nested grids is used, with a final resolution of 50 m in the targeted bays.

5.1. Karpathos, 9 February 1948

We carried out four simulations for this event which arise from the two possible fault planes of the PDFM mechanism when placed at the original ISS location and our relocated epicenter 33 km to the north. We discuss here simulation results assuming action on the fault plane dipping to the northwest (shown as the fault plane identified on the beachball mechanism in Fig. 8), with the source placed at our relocated epicenter; the other three simulations yielded similar results. Scaling laws (Geller, 1976) yield a fault length of 52 km, width of 26 km, and a slip of 1.5 m.

Fig. 8(a) shows the computed field of seafloor deformation used in the simulation; because the source depth is substantial (60 km), the vertical deformation remains small (<15 cm). Fig. 8(b) contours the

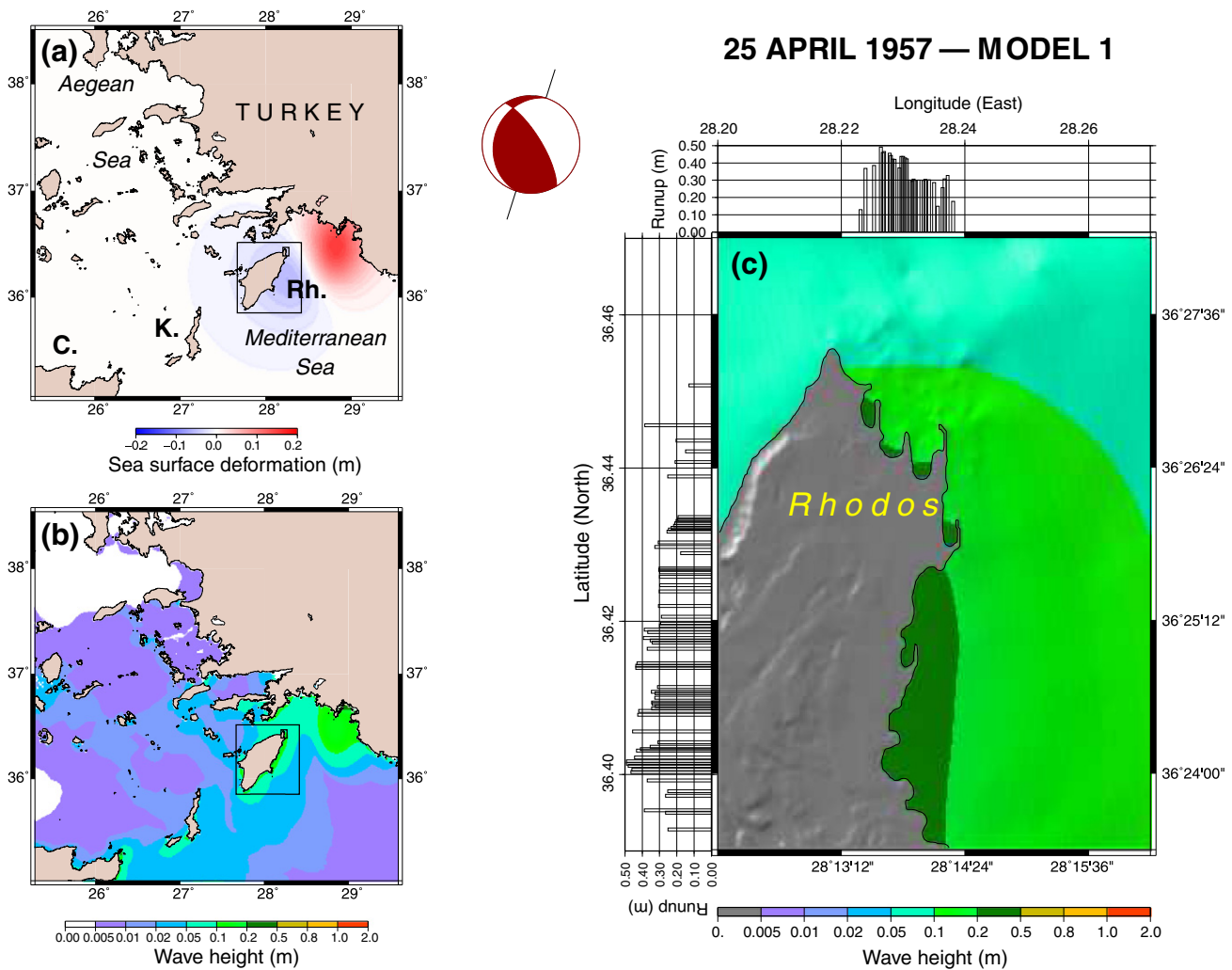


Fig. 10. Hydrodynamic simulation results for 24 April 1957 strike-slip earthquake on first fault plane of preferred focal mechanism (identified on beachball). (a) Regional vertical sea surface deformation calculated after Okada (1985) using scaled fault geometry (Geller, 1976) and inverted moment; C. = Crete; K. = Karpathos; Rh. = Rhodos. (b) Regional contour map showing maximum tsunami amplitude at each simulation point. Boxes around the island of Rhodos and surrounding the city of Rhodos in (a) and (b) represent nested grids used in simulations. (c) Contour map of maximum tsunami amplitude in highest-resolution grid, which includes city and port of Rhodos; this simulation includes run-up on initially dry land.

maximum amplitude of the wave at each point during the 4-hour simulation. As shown in Fig. 8(c) and (d), simulated tsunami run-up amplitudes do not exceed 15 cm at Diafani and 20 cm at Pigadia, each less by an order of magnitude than observed values (3 and 7 m, respectively; see Table 3 and Fig. 7). Furthermore, decreasing source depth to the shallowest depth within our range of relocation uncertainty (50 km) increases simulated run-up heights by only 20%. We thus conclude that seismic source models compatible with the inversion of the available seismic data cannot recreate the tsunami observed following the Karpathos earthquake.

Rather, we investigate whether the Karpathos tsunami can be modeled as the result of a submarine landslide triggered by the earthquake. Our source is inspired by that used by Synolakis et al. (2002) in the case of the 1998 Papua New Guinea tsunami. It consists of an asymmetric dipole featuring a ~6-m-deep trough and a ~2-m hump separated by a 10-km lever; we place the source near 35.5°N, 27.3°E, where a significant slope in bathymetry exists (see Fig. 9(a) and (b)). Fig. 9(c) and (d) show that with this source we are able to reproduce critical characteristics of the observed tsunami: a run-up of 5 m in Pigadia Bay, which reaches over 7 m at its northern and southern extremities, and a run-up of 3 to 4 m in Diafani Bay. This source also fails to significantly inundate the western coast of Karpathos (i.e. at Finiki), and creates an initial drawdown on the eastern coast. While this source may remain *ad hoc* in the absence of detailed

bathymetry at a sufficiently small scale, this experiment establishes that the surveyed tsunami measurements can be successfully modeled as resulting from a submarine landslide.

5.2. East of Rhodos, 24 and 25 April 1957

Results are presented in Figs. 10 and 11 for the first Rhodos event (strike-slip; 24 April 1957) and Figs. 12 and 13 for the second (thrust; 25 April 1957). In each of these figures, the focal plane selected as the fault plane is identified on the beachball mechanism. Subfigures (a) show the computed fields of vertical seafloor deformation; because of the relatively small size of these two earthquakes and their significant depths, the choice of focal plane has only a minor effect on deformation. Boxes in the figures around the island of Rhodos and at the northern tip of the island represent the nested grids used in the simulation. Subfigures (b) contour the maximum amplitude of the wave at each point during the 4-hour simulation. Subfigures (c) zoom in on the simulations' final and finest grid, within which the city and port of Rhodos are sampled at 50-m intervals.

In the case of the second event (25 April 1957; Figs. 12 and 13), we also show at the left and top of subfigures (c) run-up values at individual locations along the eastern coast of Rhodos, plotted as a function of latitude (to the left) or longitude (at top). In the case of the first event (24 April 1957; Figs. 10 and 11), run-up values on dry

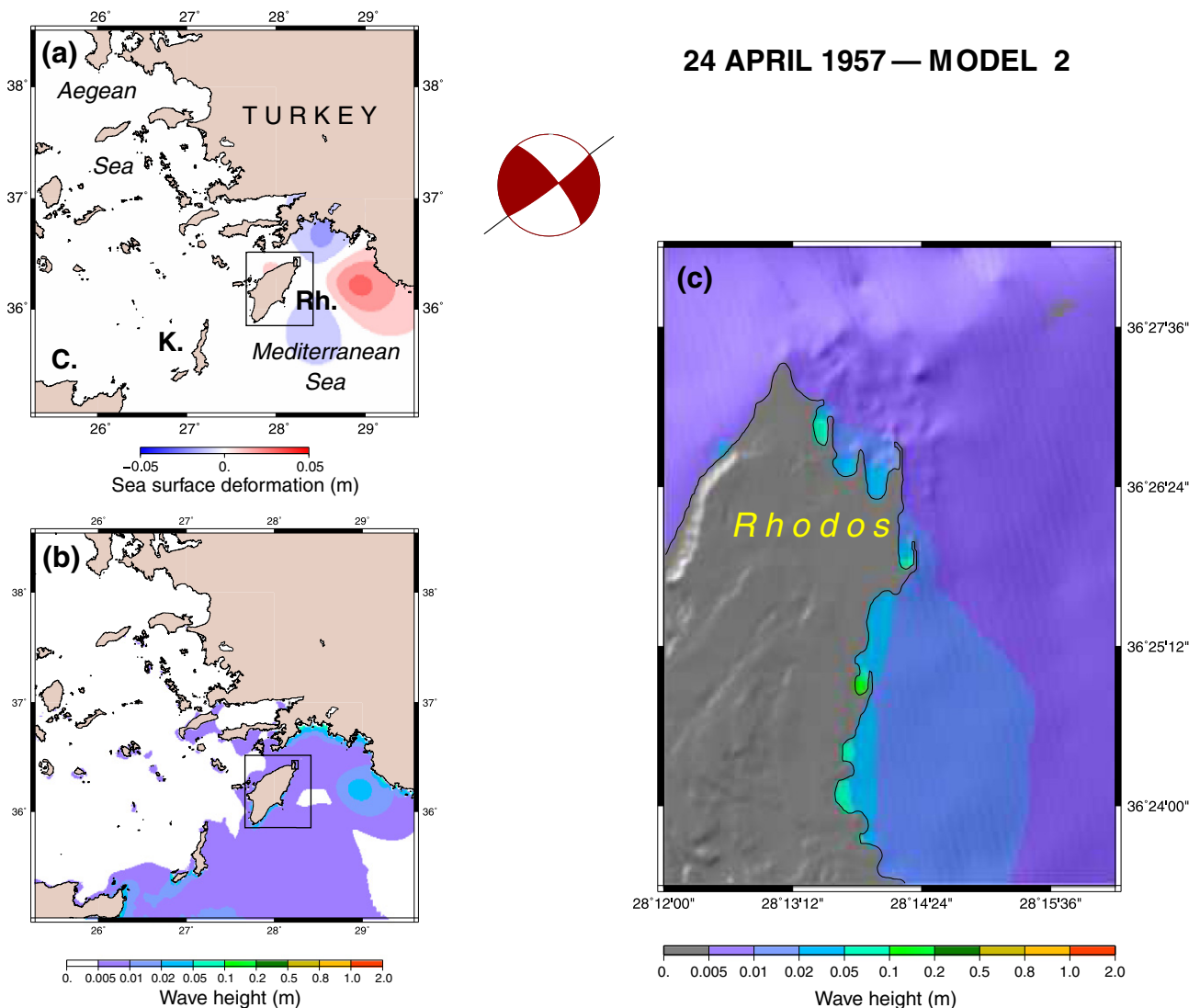


Fig. 11. Same as Fig. 10 but for earthquake on second fault plane.

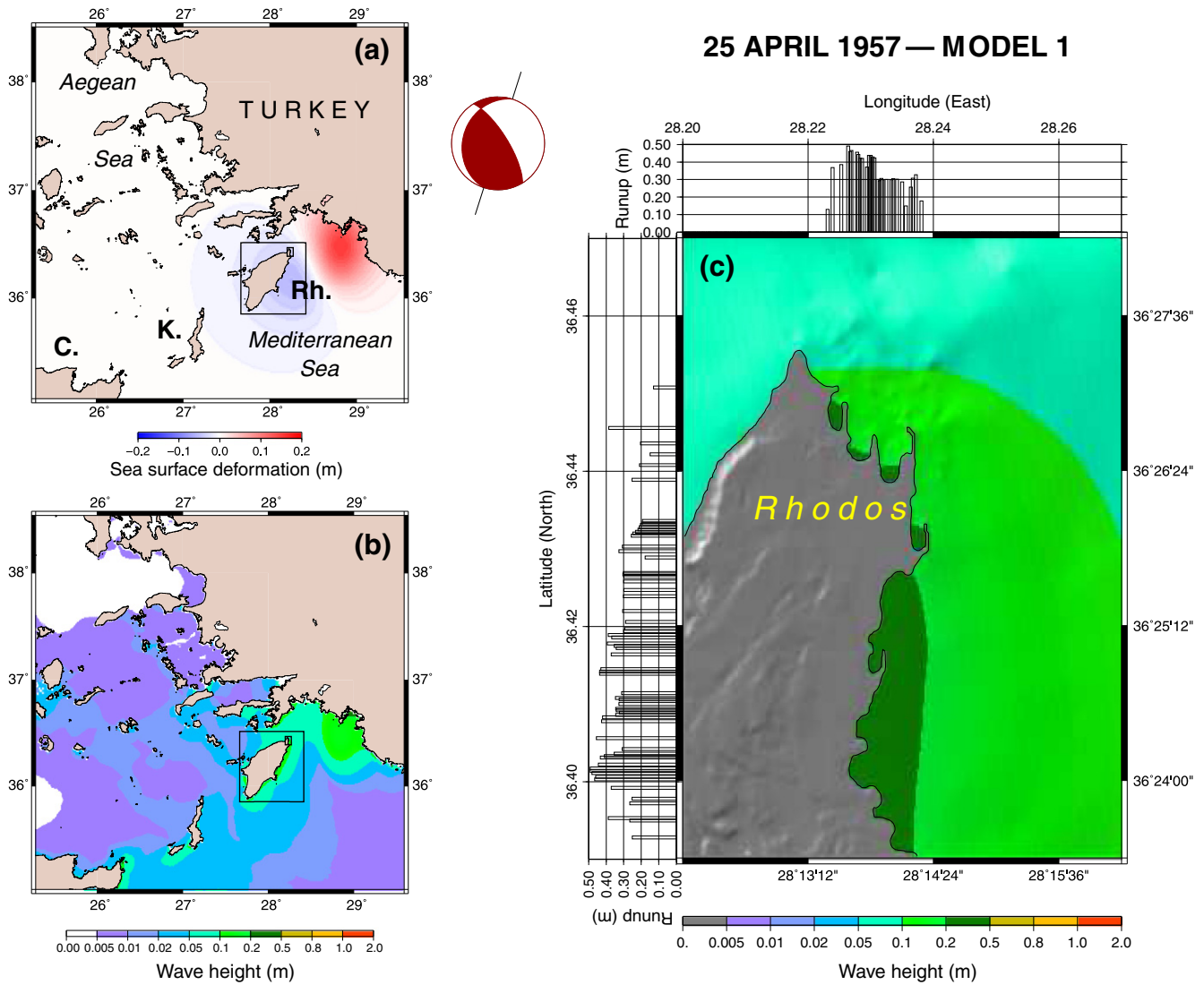


Fig. 12. Same as Fig. 10 but for 25 April 1957 thrust earthquake on first fault plane. Panels in (c) show simulated run-up amplitudes at individual locations along the eastern coast of Rhodes by latitude (left) and longitude (top).

land could not be computed, because the flow depth at the beaches always remained smaller than the altitude of the first dry point on land (typically 0.15 m), so that the wet domain was not pushed inland by the program. In lay terms, this amounts to saying that the simulation does not predict inundation of the initially dry land.

The two simulations of the second (thrusting) event predict run-up values reaching 50 cm in the southern suburbs of the city of Rhodes, and only 25 to 30 cm in the port area. These numbers suggest that the tsunami might have been observable under favorable conditions (its night-time occurrence rendered observation unlikely), but even had it been noticed, its benign character would have left no vivid memories in the minds of potential witnesses.

6. Discussion and conclusion

6.1. Seismological event reassessment

Recovered focal mechanisms for all events in this study agree broadly with the regional stress field resulting from the ongoing collision between the Nubia plate and the Aegea microplate. Our depths and focal mechanisms for the 6 October 1947 and 9 February 1948 events are consistent with earthquakes at the interface between the

subducting Nubia plate and overriding Aegea microplate. Our preferred 1947 focal mechanism indicates orthogonal convergence at the western limb of the Hellenic Arc, while the sense of motion on the northeast–southwest-trending fault plane of our preferred 1948 solution reflects left-lateral arc-oblique convergence at the eastern limb (Bohnhoff et al., 2005; LePichon and Angelier, 1979; McKenzie, 1978) and indicates full coupling between the Nubia plate and Aegea microplate (McCaffrey, 1992).

The tectonic context of the April 1957 couplet is more complicated. The progressive southward migration of the Aegea microplate boundary since the Miocene increased the curvature of the boundary and thus the obliquity of the slip vector angle (defined relative to arc-normal) in the eastern Hellenic Arc (ten Veen and Kleinspehn, 2002) such that it is $\sim 40\text{--}50^\circ$ now (Bohnhoff et al., 2005; LePichon et al., 1995). This angle exceeds that at other arcs known to partition slip (McCaffrey, 1992). In fact, the Pliny and Strabo trenches accommodate 21–23 mm/yr of sinistral motion (Kreemer and Chamot-Rooke, 2004).

Considered separately, the events of April 1957 are consistent with traditional slip partitioning in the eastern Hellenic Arc: the focal mechanism for the 24 April event has left-lateral strike-slip motion on a nearly vertical fault plane parallel to the plate boundary,

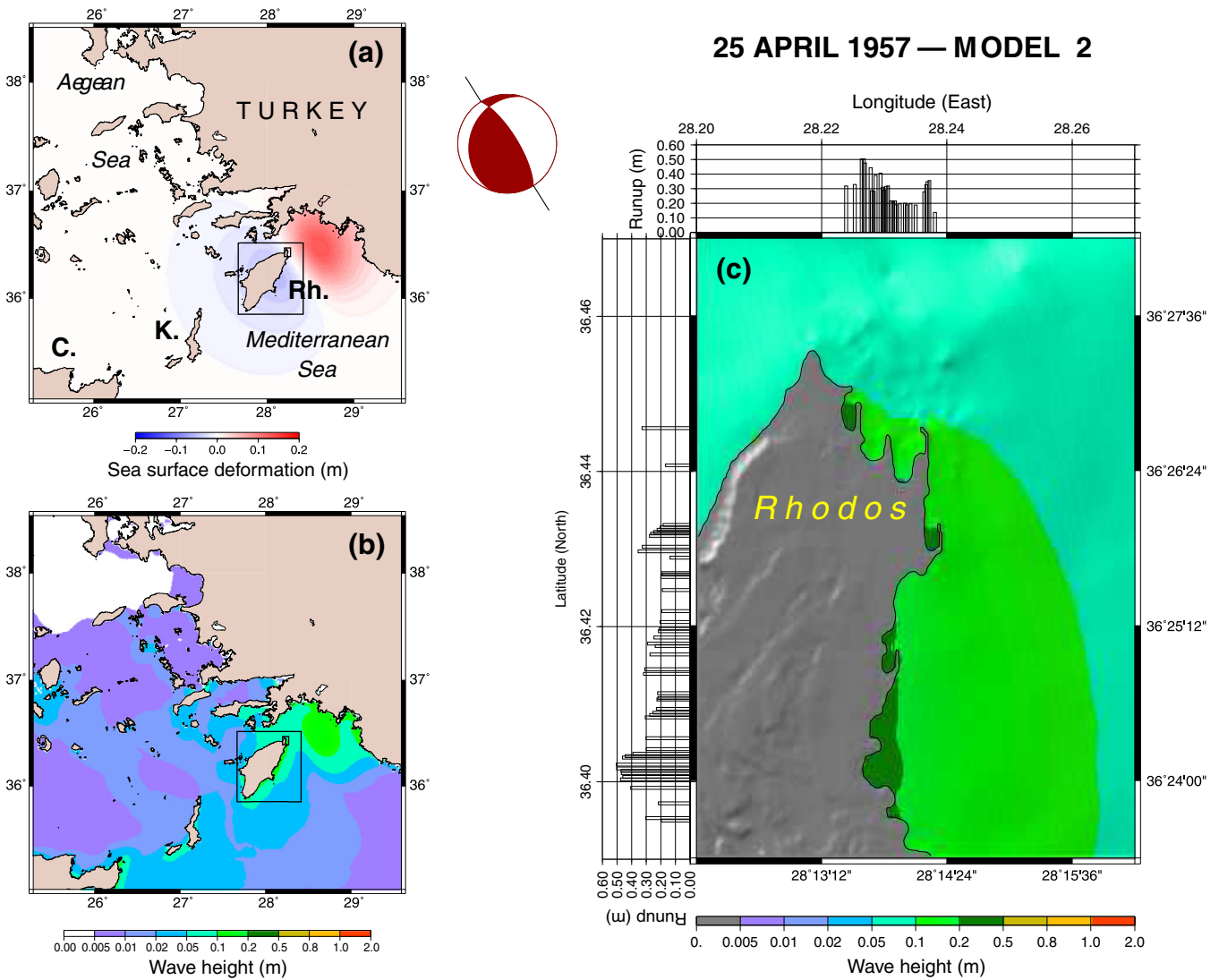


Fig. 13. Same as Fig. 12 but for earthquake on second fault plane.

while motion on the gently-dipping north–northeast–south–southwest-trending fault plane of the 25 April event demonstrates thrusting on a fault parallel to the plate boundary. But because the fault plane shared by both focal mechanism trends not parallel but oblique (north–northwest–south–southeast) to the plate boundary, the events considered together are not compatible with traditional slip partitioning.

We consider it likely that the couplet took place on the same steeply-dipping fault, because the two hypocenters relocate to essentially the same depth and lie only ~12 km apart, and because the azimuth between the two is highly similar to the strike of the common fault plane. Although the required rotation magnitude is high

compared to recent measurements of Rhodes rotation since the late Miocene (VanHinsbergen et al., 2007), we believe these events indicate non-traditional slip partitioning influenced by counter-clockwise-rotated zones of weakness generated in the past under a stress regime of differing orientation (Doutsos and Kokkalas, 2001; Hall et al., 2009).

A composite moment tensor shows that the stress field under which this couplet took place is characterized by compressional and tensional axes at plunge 29° and azimuth 47°, and at plunge 59° and azimuth 248°, respectively (an alternative focal mechanism representation is included in Table 4). The dominant contribution to the $M_0 = 1.10 \times 10^{27}$ dyn·cm composite moment tensor comes from

Table 4

Magnitude and preferred focal mechanism results. Moment M_0 from PDFM inversion; uncertainties are based on minimum and maximum moment within the centroid depth range. Moment magnitude M_w for these M_0 values after Kanamori (1977). Fault strike, dip, and slip denoted as φ , δ , and λ . The “1957 Composite” entry represents the stress field under which the 1957 April 24 and 25 event couplet took place.

Event (YYYY:JJJ)	Month	Day	M_0 ($\times 10^{27}$ dyn·cm)	M_w	φ (°)	δ (°)	λ (°)
1947:279	Oct	6	1.26 + 0.14/−0.42	7.3	302	35	91
1948:040	Feb	9	0.97 + 0.09/−0.11	7.3	100	61	115
1957:114	Apr	24	0.56 + 0.04/−0.01	7.1	53	83	14
1957:115	Apr	25	1.09 + 0.32/−0.08	7.3	328	73	71
1957 Composite	Apr	24/25	1.10	–	325	75	100

the 25 April thrust event, with only ~5% coming from the 24 April strike-slip event. A solid rotation of ~30° separates the composite tensor from that of the 25 April thrust event.

6.2. Tsunami assessment and hydrodynamic simulations

Relocated depths for the 6 October 1947 and 9 February 1948 earthquakes suggest that the associated tsunamis were likely caused by submarine landslides induced by these earthquakes rather than by the earthquakes themselves. That the event location uncertainty ellipse lies mostly on land supports this model for the 1947 tsunami. Attributing the 1948 tsunami to such a source is further supported by the inability of a modeled tectonic source compatible with the inversion of available seismic data to reproduce run-up measurements that are anomalously high for a tsunami purportedly generated by a $M_w = 7.3$ earthquake; the large-amplitude leading sea depression observed at Pigadia Bay; and the negative tsunami observation on the southwest coast of Karpathos at Finiki. In contrast, hydrodynamic simulations based on a submarine landslide source reproduce run-up values consistent with these observations.

While simulations for the 24 April 1957 strike-slip event do not predict inundations, the 25 April 1957 thrust event was capable of generating run-ups reaching up to 50 cm around Rhodos. However, there are no records of a tsunami associated with this event.

The principal conclusion of this study is that the historical tsunamis observed in the southern Aegean Sea are due to submarine landslides triggered by the respective earthquakes. This result supports the conclusion of Okal et al. (2009), who in the case of the 1956 Amorgos event demonstrated that the scattered values of extreme run-up could be explained only as resulting from co-seismically triggered underwater slumps following the main event. Even though these four events and the Amorgos event are the largest Aegean Sea earthquakes to occur during the last 100 years, on their own they fail to generate tsunamis bearing significant hazard for nearby coastlines. Notwithstanding the rare but documented occurrence of large events with a definitive direct tsunami potential, such as the 1303 southeast Aegean earthquake, this study emphasizes the hazard posed by these landslides. While detailed understanding of controlling processes remains meager, co-seismically triggered submarine landslides must be considered a significant source of regional hazard, and local populations and decision-makers must be educated about them.

Acknowledgments

We thank Dr. W. Lenhardt of the Austrian Zentralanstalt für Meteorologie und Geodynamik (ZAMG) for graciously making available analog seismograms from the Vienna (VIE) seismic station, B. Dost of KNMI for supplying seismograms from the De Bilt (DBN) seismic station, and S. Kirby and J. Dewey for access to the USGS microfilm collection in Golden, Colorado. Helpful reviews by Dr. Mian Liu and Dr. Martha Savage resulted in an improved manuscript. This work was supported by a National Science Foundation (NSF) Graduate Research Fellowship under grant no. DGE-0824162 to CWE. Landslide modeling was supported under NSF grant no. CMII-0928905 to CES. We also thank HCMR's Dr. V. Lykousis for suggestions and financial support. Some figures were generated using the Generic Mapping Tools (GMT) software (Wessel and Smith, 1991).

References

- Abe, K., 1981. Magnitudes of large shallow earthquakes from 1904 to 1980. *Physics of the Earth and Planetary Interiors* 27, 72–92.
- Altunok, Y., Ersoy, Ş., 2000. Tsunamis observed on and near the Turkish coast. *Natural Hazards* 21, 185–205.
- Ambraseys, N., 2001. Reassessment of earthquakes, 1900–1999, in the Eastern Mediterranean and the Middle East. *Geophysical Journal International* 145, 471–485.
- Ambraseys, N., Jackson, J., 1990. Seismicity and associated strain of central Greece between 1890 and 1988. *Geophysical Journal International* 101, 663–708.
- Ambraseys, N., Synolakis, C., 2010. Tsunami catalogs for the Eastern Mediterranean, revisited. *Journal of Earthquake Engineering* 143, 309–330.
- Benetatos, C., Kiratzi, A., Papazachos, C., Karakaisis, G., 2004. Focal mechanisms of shallow and intermediate depth earthquakes along the Hellenic Arc. *Journal of Geodynamics* 37, 253–296.
- Bohnhoff, M., Harjes, H.-P., Meier, T., 2005. Deformation and stress regimes in the Hellenic subduction zone from focal mechanisms. *Journal of Seismology* 9, 341–366.
- Charlier, C., van Gils, J.-M., 1953. Liste des stations sismologiques mondiales. Obs. R. Belg. Uccle.
- Doutsos, T., Kokkalas, S., 2001. Stress and deformation patterns in the Aegean region. *Journal of Structural Geology* 23, 455–472.
- Ekström, G., 1987. A Broad Band Method of Earthquakes Analysis. Ph.D. Thesis, Harvard University, Cambridge, MA.
- El-Sayed, A., Romanelli, F., Panza, G., 2000. Recent seismicity and realistic waveform modeling to reduce ambiguities about the 1303 seismic activity in Egypt. *Tectonophysics* 328, 341–357.
- Galanopoulos, A., 1949. The Koroni (Messinia) earthquake of October 6, 1947. *Bulletin of the Seismological Society of America* 391, 33–39.
- Geller, R., 1976. Scaling relations for earthquake source parameters and magnitudes. *Bulletin of the Seismological Society of America* 66, 1501–1523.
- Guidoboni, E., Comastri, A., 1997. The large earthquake of 8 August 1303 in Crete: seismic scenario and tsunami in the Mediterranean area. *Journal of Seismology* 1, 55–72.
- Gutenberg, B., Richter, C., 1954. *Seismicity of the Earth and Associated Phenomena*. Hafner Publishing Company, New York and London.
- Hall, J., Aksu, A., Yalıtırak, C., Winsor, J., 2009. Structural architecture of the Rhodes Basin: a deep depocentre that evolved since the Pliocene at the junction of the Hellenic and Cyprus arcs, eastern Mediterranean. *Marine Geology* 258, 1–23.
- Jackson, J., 1994. Active tectonics of the Aegean region. *Annual Review of Earth and Planetary Sciences* 22, 239–271.
- Jongsma, D., 1977. Bathymetry and shallow structure of the Pliny and Strabo Trenches, south of the Hellenic Arc. *Geological Society of America Bulletin* 88, 797–805 June.
- Kanamori, H., 1977. The energy release in large earthquakes. *Journal of Geophysical Research* 82, 2981–2987.
- Kiratzi, A., Louvari, E., 2003. Focal mechanisms of shallow earthquakes in the Aegean Sea and the surrounding lands determined by waveform modelling: a new database. *Journal of Geodynamics* 36, 251–274.
- Kiratzi, A., Papazachos, C., 1995. Active crustal deformation from the Azores triple junction to the Middle East. *Tectonophysics* 243, 1–24.
- Kreemer, C., Chamot-Rooke, N., 2004. Contemporary kinematics of the southern Aegean and the Mediterranean Ridge. *Geophysical Journal International* 157, 1377–1392.
- LePichon, X., Angelier, J., 1979. The Hellenic Arc and trench system: a key to the neotectonic evolution of the eastern Mediterranean area. *Tectonophysics* 60, 1–42.
- LePichon, X., Chamot-Rooke, N., Lallemand, S., 1995. Geodetic determination of the kinematics of central Greece with respect to Europe: implications for eastern Mediterranean tectonics. *Journal of Geophysical Research* 100B7, 12,675–12,690.
- Makropoulos, K., 1978. The Statistics of Large Earthquake Magnitude and an Evaluation of Greek Seismicity. Ph.D. Thesis, University of Edinburgh, Edinburgh.
- Makropoulos, K., Burton, P., 1981. A catalogue of seismicity in Greece and adjacent areas. *Geophysical Journal of the Royal Astronomical Society* 65, 741–762.
- McCaffrey, R., 1992. Oblique plate convergence, slip vectors, and forearc deformation. *Journal of Geophysical Research* 97B6, 8905–8915 June.
- McClusky, S., Balassanian, S., Barka, A., Demir, C., Ergintav, S., Georgiev, I., Gurkan, O., Hamburger, M., Hurst, K., Kahle, H., Kastens, K., Kekelidze, G., King, R., Kotzev, V., Lenk, O., Mahmoud, S., Mishin, A., Nadariya, M., Ouzounis, A., Paradissis, D., Peter, Y., Prilepin, M., Reilinger, R., Sanli, I., Seeger, H., Tealeb, A., Toksöz, M., Veis, G., 2000. Global positioning system constraints on plate kinematics and dynamics in the eastern Mediterranean and Caucasus. *Journal of Geophysical Research* 105B3, 5695–5719 March.
- McClusky, S., Reilinger, R., Mahmoud, S., Sari, D., Tealeb, A., 2003. GPS constraints on Africa (Nubia) and Arabia plate motions. *Geophysical Journal International* 155, 126–138.
- McKenzie, D., 1972. Active tectonics of the Mediterranean region. *Geophysical Journal of the Royal Astronomical Society* 30, 109–185.
- McKenzie, D., 1978. Active tectonics of the Alpine-Himalaya belt: the Aegean Sea and surrounding regions. *Geophysical Journal of the Royal Astronomical Society* 55, 217–254.
- Okada, Y., 1985. Surface deformation due to shear and tensile faults in a half-space. *Bulletin of the Seismological Society of America* 754, 1135–1154.
- Okal, E., Reymond, D., 2003. The mechanism of great Banda Sea earthquake of 1 February 1938: applying the method of preliminary determination of focal mechanism to a historical event. *Earth and Planetary Science Letters* 216, 1–15.
- Okal, E., Synolakis, C., Uslu, B., Kalligeris, N., Voukouvalas, E., 2009. The 1956 earthquake and tsunami in Amorgos. *Geophysical Journal International* 178, 1533–1554.
- Papadopoulos, G., Chalkis, B., 1984. Tsunamis observed in Greece and the surrounding area from antiquity up to the present times. *Marine Geology* 56, 309–317.
- Papadopoulos, G., Kondopoulou, D., Leventakis, G.-A., Pavlides, S., 1986. Seismotectonics of the Aegean region. *Tectonophysics* 124, 67–84.
- Papadopoulos, G., Dashkalaki, E., Fokaefs, A., Giraleas, N., 2007. Tsunami hazards in the Eastern Mediterranean: strong earthquakes and tsunamis in the east Hellenic Arc and trench system. *Natural Hazards and Earth System Sciences* 7, 57–64.
- Papazachos, B., 1996. Large seismic faults in the Hellenic Arc. *Annali di Geofisica* 395, 891–903.
- Papazachos, B., Delibasis, N., 1969. Tectonic stress field and seismic faulting in the area of Greece. *Tectonophysics* 73, 231–255.

- Papazachos, B., Papadimitriou, E., Kiratzi, A., Papazachos, C., 1997. The stress field in the Aegean area as deduced from fault plane solutions of shallow earthquakes. IASPEI 29th General Assembly, Thessaloniki. . 18–28 August 1997.
- Papazachos, B., Papaioannou, C., Papazachos, C., Savvaidis, A., 1999. Rupture zones in the Aegean region. *Tectonophysics* 308, 205–221.
- Papazachos, B., Karakostas, V., Papazachos, C., Scordilis, E., 2000. The geometry of the Wadati-Benioff zone and lithospheric kinematics in the Hellenic Arc. *Tectonophysics* 319, 275–300.
- Reilinger, R., McClusky, S., Vernant, P., Lawrence, S., Ergintav, S., Cakmak, R., Ozener, H., Kadirov, F., Guliev, I., Stepanyan, R., Nadariya, M., Hahubia, G., Mahmoud, S., Sakr, K., ArRajehi, A., Paradissis, D., Al-Aydrus, A., Prilepin, M., Guseva, T., Evren, E., Dmitrova, A., Filikov, S., Gomez, F., Al-Ghazzi, R., Karam, G., 2006. GPS constraints on continental deformation in the Africa–Arabia–Eurasia continental collision zone and implications for the dynamics of plate interactions. *Journal of Geophysical Research* 111B05411.
- Reymond, D., Okal, E., 2000. Preliminary determination of focal mechanisms from the inversion of spectral amplitudes of mantle waves. *Physics of the Earth and Planetary Interiors* 121, 249–271.
- Ritsema, A., 1974. Earthquake mechanisms of the Balkan region. Tech. Rep. REM/70/172, UNDP/UNESCO Report on Survey of the Seismicity of the Balkan Region.
- Romanowicz, B., Suárez, G., 1983. On an improved method to obtain the moment tensor and depth of earthquakes from the amplitude spectrum of Rayleigh waves. *Bulletin of the Seismological Society of America* 736, 1513–1526 December.
- Soloviev, S., 1990. Tsunamigenic zones in the Mediterranean Sea. *Natural Hazards* 3, 183–202.
- Synolakis, C., Okal, E., 2005. 1992–2002: perspective on a decade of post-tsunami surveys. In: Satake, K. (Ed.), *Tsunamis: Case studies and Recent Developments: Adv. Natur. Technol. Hazards*, Vol.3, pp. 1–30.
- Synolakis, C., Bardet, J., Borrero, J., Davies, H., Okal, E., Silver, E., Sweet, S., Tappin, D., 2002. The slump origin of the 1998 Papua New Guinea Tsunami. *Proceedings of the Royal Society of London Series A* 4582020, 763–789 April.
- ten Veen, J., Kleinspehn, K., 2002. Geodynamics along an increasingly curved convergent plate margin: Late Miocene–Pleistocene Rhodes, Greece. *Tectonics* 213.
- Titov, V., Synolakis, C., 1998. Numerical modeling of tidal wave runup. *Journal of Waterway Port, Coastal, and Ocean Engineering* 124, 17–171.
- VanHinsbergen, D., Krijgsman, W., Langereis, C., Cornee, J.-J., Duermeijer, C., VanVugt, N., 2007. Discrete Plio-Pleistocene phases of tilting and counterclockwise rotation in the southeastern Aegean arc (Rhodos, Greece): Early Pliocene formation of the south Aegean left-lateral strike-slip system. *Journal of the Geological Society of London* 164, 1133–1144.
- Wessel, P., Smith, W., 1991. Free software helps map and display data. *Eos Transactions of the American Geophysical Union* 72441.
- Wysession, M., Okal, E., Miller, K., 1991. Intraplate seismicity of the Pacific Basin. *Pure and Applied Geophysics* 135, 261–359.